ELSEVIER

Fluid Dynamics Research 31 (2002) 185–213

FLUID DYNAMICS RESEARCH

Numerical modelling of hydraulic jumps in a spiral channel with rectangular cross section

Wolfgang Schacht[a,*], Evgenii V. Vorozhtsov[b], Anatoly F. Voevodin[c], Vladimir V. Ostapenko[c]

[a] *Am Hankelsberg 21, 07778 Dorndorf-Steudnitz, Germany*
[b] *Institute of Theoretical and Applied Mechanics, Russian Academy of Sciences, Novosibirsk 630090, Russia*
[c] *Institute of Hydrodynamics, Russian Academy of Sciences, Novosibirsk 630090, Russia*

Received 14 May 2001; received in revised form 29 May 2002; accepted 26 June 2002

Abstract

We present two finite difference methods for numerical modelling of nonstationary compressible fluid flows in a spiral channel with rectangular cross section. One of these methods is an explicit TVD scheme. Another scheme uses splitting in terms of physical processes and an implicit approximation of the friction term. The implemented numerical methods serve not only for computation of the damping of pressure jumps and evaluation of pressure compensators in percussion–rotary drilling devices but are also of great methodical and practical importance for the treatment of such flow problems.

Keywords: Finite difference scheme; Compressible flow; Shocks; Friction term

1. Introduction

Percussion drilling is the oldest technique for the drilling of wells. It has a low drilling velocity and is used at present only in particular cases. Since the middle of the 19th century, rotary drilling had been introduced in practice, which had undergone many improvements since then. At present, the percussion–rotary technique of well drilling for exploration drilling and oil and natural gas production is the predominant technique of drilling. The percussion–rotary drilling is a combination of the rotary and percussion methods and has the following advantages over the pure rotary drilling:

- higher drilling velocity in moderately hard and hard stone;

* Corresponding author. Fax: +49-036427-22830.
E-mail address: dr_schacht@t-online.de (W. Schacht).

0169-5983/02/$22.00
PII: S0169-5983(02)00104-1

- better stability of well direction and
- insignificant wear because of lesser rotation frequency and lesser drilling pressure.

In the next section we explain how a hydraulic drilling hammer works. One of the features of the fluid flow processes occurring within this device is the formation of shock waves. The pressure behind the shock wave fronts in the hydraulic drilling hammer may take very large values. On the one hand, the shock efficiency of the drilling hammer can be increased by an efficient use of such shock waves. On the other hand, the shocks may lead to the destruction of the drilling device under unfavourable hydraulic conditions. A design goal of the drilling technology is to reduce the strength of shocks propagating in the direction opposite to fluid flow by mounting the appropriate pressure compensators, and to maximally use the shocks in the direction of anvil and drill bit for the drilling process. For an optimal design and scaling of such pressure compensators, the mathematical modelling of nonstationary flow processes in spiral compensators is of great practical importance. Despite this fact, there were until now no attempts of modelling the flow in the channel on the basis of approximate numerical solution of partial differential equations of fluid mechanics.

The choice of the mathematical model for the solution of a specific fluid flow problem is strongly affected by the values of the fluid Mach numbers, which are typical of the fluid flow problem under consideration. In the case of fluid flow in spiral compensators, the typical Mach number values do not exceed 0.03. Therefore, one might think that the model of inviscid incompressible fluid would be more efficient for the numerical modelling of such fluid flows. It is, however, not clear how one can perform a mathematically correct modelling of the propagation of nonstationary hydraulic jumps within the incompressible fluid model.

Jacob (1977), Swaffield and Boldy (1993) and Zhao (1998) considered the numerical modelling of nonstationary fluid flow processes in percussion–rotary drills. Such flows were modelled by Swaffield and Boldy (1993) and Zhao (1998) in one-dimensional approximation with the aid of the method of characteristics.

In connection with the foregoing, we base our numerical modelling of fluid flow processes in spiral compensators on the inviscid compressible fluid model. As a working liquid, distilled water is used in percussion–rotary drilling devices. As was shown, for example, by Swaffield and Boldy (1993), the barotropic fluid model describes satisfactorily the water behaviour under the pressures typical of percussion–rotary drills. In this connection, we use in the present work the mathematical model of a barotropic compressible inviscid fluid for modelling of the flow processes in spiral compensators of the percussion–rotary drilling devices. Owing to the use of the barotropic fluid assumption, this mathematical model involves in the one-dimensional case only two partial differential equations: the continuity equation and the momentum equation. At the same time, the well-known Euler equations for flows of ideal compressible fluids involve three equations (the first two equations are the continuity and momentum equations, and the third equation is the energy equation).

It is desirable to carry out the mathematical description of nonstationary fluid flow in a spiral channel with rectangular cross section with regard to curved walls, which cause a complex propagation and reflection of shock waves as well as centrifugal forces, by using a three-dimensional model. For the development and analysis of such a complex model, big research work as well as computer time expenses are needed. In this connection, it is advisable to reduce at the first stage

the investigation of fluid flow in a spiral channel with regard to important model parameters to a one-dimensional flow problem.

One can use the method of characteristics as well as the finite difference methods for numerical modelling of such a one-dimensional nonstationary flow in a rectangular channel. With regard to a subsequent generalization of the one-dimensional computational model for the case of a two- and three-dimensional flow the present authors have decided to use the finite difference method. Although the method of characteristics is well suited for the description of one-dimensional pressure shocks, it has not gained widespread acceptance at the numerical modelling of two- and three-dimensional fluid dynamics problems because of many types of possible interactions and singularities arising at the intersection of characteristic surfaces (Roache, 1976).

We present two finite difference methods for the numerical solution of the problem of barotropic fluid flow in spiral compensator. Despite the fact that we use the barotropic fluid model, the solution of the task under consideration has proved sufficiently laborious already in the one-dimensional case. One of the reasons for this is the need to perform several thousands of time steps in order to obtain reliable predictions of the pressure behaviour at the upper outlet of the spiral compensator. Another difficulty is caused by the friction term in the momentum equation. It turns out that this source term is a moderately stiff source term, which may lead to the overshoots in the numerical solution behind the shock wave fronts when a TVD scheme is used. We show how the free parameters available in the TVD scheme should be chosen in order to eliminate this undesirable effect.

The paper is organized as follows. In Section 2 we describe in detail the physical processes, which take place in the hydraulic drilling hammer during its single working cycle. In Section 3 we obtain the constraints for geometric parameters of the spiral compensator with regard to technological design requirements. In Section 4 we present the governing equations for one-dimensional barotropic compressible fluid flow in the presence of fluid friction on the channel walls. In Section 5 we present two numerical schemes and discuss the difficulties related to the dispersion effect of the friction term. In Section 6 we present the numerical results on the validation of both difference methods and then apply the numerical methods for the modelling of flow processes in actual spiral compensators. In Section 7 we formulate the conclusions.

2. Process description

The hydraulic drilling hammer (Fig. 1) consists of the shock piston (1), anvil (2) and drill bit (3) as well as a valve (4) with a spring (5).

The fluid enters from above via the valve (4), which moves depending on the volume rate against the spring strength downwards, and then the fluid flows through the shock piston (1), which has a larger frontal surface at the lower fluid outlet than at the inlet, into the space I via the channel in the anvil.

Since the lower frontal surface of the shock piston (1) is larger than its upper frontal surface, a larger pressure develops on the lower frontal surface than on the upper frontal surface of the piston. Because of this difference in pressures the shock piston (1) moves upwards and finally leads to a sudden interruption of flow when its upper frontal surface encounters the valve (4). This results in a pressure shock (also called shock wave), which accelerates the valve (4) motion as well as the downward motion of shock piston (1). Then it again frees, however, the flow at the lower dead

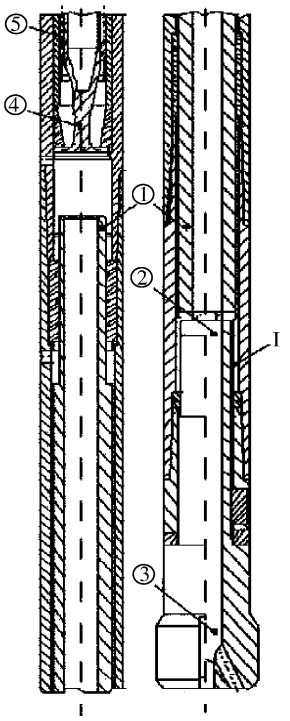

Fig. 1. The percussion–rotary drilling device.

point of the valve (4). The piston (1) hits due to its inertia the anvil (2), and the above process repeats again.

When the valve (4) is closed the shock wave forms above the valve, which then propagates in the spiral compensator (shown in Fig. 2) upwards. After the shock wave already damped in the spiral compensator has left the spiral compensator it propagates further upwards in a pipeline and enters a reservoir which is used as a pressure accumulator of the pump. Thus, the shock wave propagates in the spiral compensator in the direction opposite to the fluid flow. The purpose of the spiral compensator is to damp the periodical shock waves, which could destruct both the drilling device and the pipeline supplying the fluid to the percussion–rotary drill.

Fig. 2 shows a typical actual spiral compensator of the drilling unit; the compensator diameter is $4\ \frac{3}{4}$ in, and the drilling unit produces a borehole 6 in in diameter.

We now explain the way in which the fluid flows through the drilling device. Inside the drilling hammer the fluid flows downwards. The drill bit (3) is supplied with inclined nozzles through which the fluid leaves the drilling hammer and then flows, together with stone crumb produced as a result of drilling, upwards. The inclined positioning of the nozzles in the drill bit ensures that the drill bit (3) turns by a certain angle (percussion–rotary drilling) after each impact of the piston (1) against the anvil (2). Due to the high frequency of the impacts the mixture of fluid and stone crumb flows rather continuously upwards (6). The path of the fluid (which subsequently carries the crumb) is shown in Fig. 1 by the dashed lines supplied with arrows.

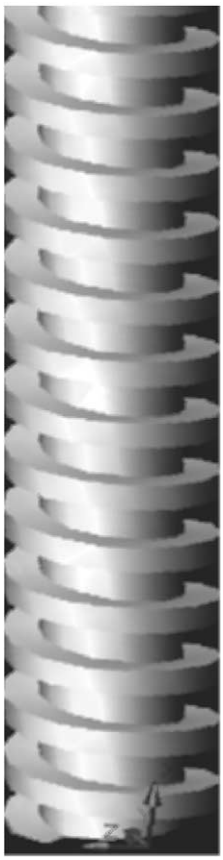

Fig. 2. Spiral compensator.

3. Geometrical constraints

As we will see in this section the nondimensionalized equations (20) for fluid flow in a spiral channel involve the length L of the channel (it enters both the friction term and the term taking into account the gravity force effect). Therefore, the channel length affects directly the damping of shock waves in the process of their propagation along the channel. This effect can be quite significant if the channel length is sufficiently large. For example, we have conducted a number of numerical experiments for the cases in which the length of a hypothetical spiral channel exceeded the length of the channel of an actual spiral compensator by a factor from two to four. As a result, we were able to reduce the fluid pressure amplitude at the upper outlet of the compensator by a factor of about two in comparison with the pressure amplitude at the lower inlet of the spiral compensator.

But since we are going to investigate the effects of the damping of pressure surges in actual compensators, we must take into account the length L of these compensators at the numerical modelling. Therefore, before proceeding to the presentation of the fluid mechanics equations governing the one-dimensional fluid flow in spiral channel we at first derive the needed formula for the length L of the spiral channel of actual compensator.

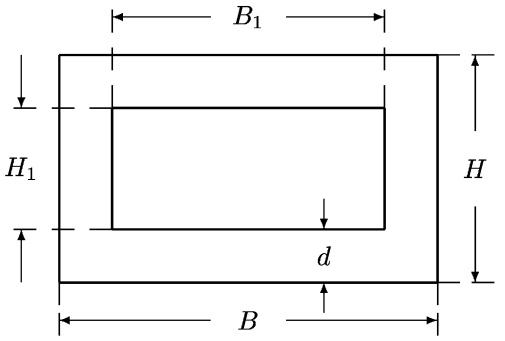

Fig. 3. The rectangular cross section of a spiral channel.

Let us consider a spiral, which runs spatially on the surface of a circular cylinder. The parameter equations of this line are as follows (Bushgens, 1940; Blaschke, 1950):

$$x_0(s) = a\cos s, \quad y_0(s) = -a\sin s, \quad z_0(s) = c_1 s, \quad 0 \leqslant s \leqslant s_{\max}, \tag{1}$$

where s is the parameter, a is the radius of the cylinder curve and c_1 is a coefficient, which will be defined precisely below in this section.

The minus sign appears in the expression for $y_0(s)$ in (1) because the spiral of actual compensator runs on the cylinder surface in clockwise manner from bottom to top, see Fig. 2.

At all points of spiral, the curvature and torsion are constant. The length of a piece of spiral between two points lying one over the other is called a turn, and the vertical distance between them is called the flank pitch.

We will consider in the following Eqs. (1) as the equations for the central line or the axis of the spiral channel, that is the line which is a locus of the geometric centres of the rectangular cross sections obtained in the planes $s = \text{const}$.

The existing designs of spiral compensators have a number of constraints for their geometric dimensions:

(i) the height $z_{\max}$ of the cylinder on whose surface the central line (1) of the spiral channel lies does not exceed 0.9 m and lies within the range $0.4\text{ m} \leqslant z_{\max} \leqslant 0.9\text{ m}$;

(ii) the external radius $a + B$ does not exceed 0.2 m, where B is the external horizontal size of the channel cross section (see Fig. 3);

(iii) the thickness of the spiral channel wall is of the order 0.01 m.

Within the framework of existing limitations for the dimensions of spiral compensators it is possible to vary the spiral channel length L at the expense of the specification of a flank pitch, the central line radius a, and the value of B. Let us now find the channel length L as a function of the technological constraints for the dimensions of the spiral channel.

If we denote the vertical distance between a single turn by Δz, then it is obvious that $\Delta z \geqslant H$ is one condition for a spiral channel, where H is the external vertical size of the cross section of the spiral channel, see Fig. 3. Since Δz is an increment of the z coordinate after each turn, one can formulate the relation $c_1 2\pi \geqslant H$ as a constraint for the coefficient c_1 in (1). For practical

computations, we have used the relation

$$c_1 = \frac{\psi H}{2\pi}, \tag{2}$$

where the factor $\psi \geqslant 1$ is to be determined with regard to dimension constraints.

Since line (1) is assumed to be the central line of a spiral channel, we will assume that at $s = 0$ the inequality $z_0(s) \geqslant H/2$ is satisfied. We obtain the following inequality from the requirement that the spiral compensator height does not exceed the value $z_{\max}$: $c_1 s \leqslant z_{\max} - H$.

Substituting expression (2) for c_1 into this inequality, we obtain

$$s \leqslant \frac{z_{\max} 2\pi}{\psi H} - \frac{2\pi}{\psi}. \tag{3}$$

If in addition it is required that at least one complete turn of spiral is projected onto the plane $z = 0$ (the number of turns in a spiral compensator is always larger than 1), then the following inequality is obtained from constraint (3):

$$\frac{z_{\max} \cdot \pi}{\psi H} - \frac{\pi}{\psi} \geqslant \pi. \tag{4}$$

If the values of $z_{\max}$ and H are known, then one can obtain from (4) also the constraint

$$\frac{\pi \cdot z_{\max}}{H} - \pi \geqslant \pi \cdot \psi,$$

or

$$1 \leqslant \psi \leqslant \frac{z_{\max}}{H} - 1. \tag{5}$$

Denote by α the angle between the spiral tangent and the vector of gravity force. By using the elementary methods it is easy to obtain the following equation for the determination of angle α:

$$\sin(\alpha) = \sqrt{1 - \cos^2(\alpha)} = \frac{a}{\sqrt{a^2 + c_1^2}} = \text{const}. \tag{6}$$

According to (5) the maximum value of ψ is

$$\psi_{\max} = (z_{\max}/H) - 1. \tag{7}$$

Let us denote by $c_{1,\max}$ the maximum admissible value of coefficient c_1 in (1). Then, in accordance with (2) and (7),

$$c_{1,\max} = \psi_{\max} \frac{H}{2\pi} = \frac{H}{2\pi}\left(\frac{z_{\max}}{H} - 1\right) = \frac{z_{\max}}{2\pi} - \frac{H}{2\pi}. \tag{8}$$

Since the coefficient c_1 should always satisfy the constraint $c_1 \leqslant c_{1,\max}$ in order to ensure the inequality $c_1 s \leqslant z_{\max} - H$, we obtain, by elementary proof, the inequality

$$\sin\alpha = \frac{1}{\sqrt{1 + c_1^2/a^2}} \geqslant \frac{1}{\sqrt{1 + c_{1,\max}^2/a^2}}.$$

The least admissible value $c_{1,\min}$ of coefficient c_1 in (1) is obtained from (2) at $\psi = 1$: $c_{1,\min} = H/(2\pi)$. Denote by $\alpha_{\min}$ and $\alpha_{\max}$ the least and largest admissible values of the angle α in (6). Then it is

obvious that

$$\alpha_{\min} = \arcsin\left(\frac{a}{\sqrt{a^2 + c_{1,\max}^2}}\right), \quad \alpha_{\max} = \arcsin\left(\frac{2\pi a}{\sqrt{4\pi^2 a^2 + H^2}}\right). \tag{9}$$

Thus, we have found that one can vary the angle α within the interval $\alpha_{\min} \leqslant \alpha \leqslant \alpha_{\max}$, and this will not lead to the violation of the constraint for the vertical size of spiral compensator. We can efficiently take into account these constraints for α in the computer code for the optimization of the spiral compensator design by specifying the angle α as follows:

$$\alpha = \alpha_{\min} + \psi_1(\alpha_{\max} - \alpha_{\min}), \tag{10}$$

where ψ_1 is a user-specified coefficient lying in the range $0 \leqslant \psi_1 \leqslant 1$.

After the angle α has been specified, one can determine the coefficient c_1 with the aid of Eq. (6). It follows from (6) that $\sin^2(\alpha) = a^2/(a^2 + c_1^2)$, so that we obtain for c_1 the formula $c_1 = a\cot(\alpha)$. The value of ψ is then determined from (2). This value enables us to formulate the admissible constraints for the parameter s: $0 \leqslant s \leqslant s_{\max}$, where $s_{\max} = (2\pi/\psi)((z_{\max}/H) - 1)$ with regard to (3).

Finally one can calculate with the aid of quantity $s_{\max}$ the total length of the spiral channel:

$$L = \int_0^{s_{\max}} [(x_s')^2 + (y_s')^2 + (z_s')^2]^{0.5} ds = \sqrt{a^2 + c_1^2} \cdot s_{\max}. \tag{11}$$

Formula (11) will be used below for the one-dimensional computation of nonstationary fluid flow in spiral channel with rectangular cross section see Eqs. (20).

4. Governing equations

The nonstationary flow in the spiral channel under study is characterized by the presence of shock waves. For the mathematical description of such a flow the conservation laws are formulated for mass and momentum in divergence form (Rožděstvenskii and Yanenko, 1983; Voevodin and Shugrin, 1981):

$$\frac{\partial \rho}{\partial t} + \frac{\partial \rho w}{\partial x} = 0, \tag{12}$$

$$\frac{\partial \rho w}{\partial t} + \frac{\partial \rho w^2 + p}{\partial x} = -\rho g \cos(\alpha) - \rho \frac{\lambda}{2D} |w| w. \tag{13}$$

In Eqs. (12) and (13) ρ is the fluid density, w is the velocity, p is the pressure, and g is the acceleration due to gravity (9.81 m/s^2). The computational formula for the angle α between the spiral tangent and the vector of gravity force was already derived above, see (10).

To close Eqs. (12) and (13) the equation of state for fluids

$$p = K_{\text{eff}} \ln(\rho/\rho_0) \tag{14}$$

is needed. The constant K_{eff}, which is also known in the literature as bulk modulus, may be computed for a rectangular channel as follows (Jenkner, 1971):

$$K_{\text{eff}} = \frac{1}{1/E_{\text{F}} + (B/H)^4 R(\beta)/15(d/H)^3 E_{\text{M}}}, \tag{15}$$

where E_F and E_M are Young's modules of elasticity for fluid and wall material, respectively, d is the wall thickness, and B or H are the external dimensions of the channel cross section. The quantity $R(\beta)$ is the so-called rectangular factor:

$$R(\beta) = \frac{1}{2}(6 - 5\beta) + \frac{1}{2}\left(\frac{H}{B}\right)^5 \left(6 - 5\beta\left(\frac{B}{H}\right)^2\right), \quad \beta = 1 - \frac{H}{B} + \left(\frac{H}{B}\right)^2. \tag{16}$$

A check-up of the derivation of these formulas by the present authors has resulted in the conclusion that it is necessary to slightly correct expression (15). It has the following form for the task to be solved:

$$K_{\text{eff}} = \frac{1}{1/E_F + (B/H)^4 R(\beta)/10(d/H)^3 E_M}. \tag{17}$$

The term $\rho\lambda|w|w/(2D)$ in Eq. (13) takes into account the losses due to wall friction in channel. A number of different computational formulas for the wall friction number λ were proposed by Abramovich (1991) for the case of a stationary flow as functions of the Reynolds number and the relative wall roughness. Because of the periodic shock waves the flow in a spiral rectangular channel is strongly nonstationary. Therefore, we have used in the present work the following relations based on the experimental data,

$$D = \frac{B_1 H_1}{B_1 + H_1}, \qquad \lambda = \frac{0.021}{D^{0.3}} \tag{18}$$

for the computation of the effective diameter D and the wall friction number λ (Merenkov et al., 1992). Here B_1 and H_1 are the internal dimensions of flow channel (see Fig. 3).

At the propagation of periodic shock waves, the regions with very low pressure may arise, which may lead to cavity phenomena (Swaffield and Boldy, 1993; Zhao, 1998). Such phenomena can, in principle, be modelled and investigated within the framework of the one-dimensional model. Zhao (1998) has proposed a simplified cavity model, in which the fluid column is separated into two equal columns by a bubble filled with saturated vapour. A substantially more exact model would be a model in which a transition zone is defined and in which gas bubbles are formed (Abramovich, 1991).

A simplified method for the treatment of cavities is also applied in the subsequent computations. It is based, as the governing partial differential equations (12) and (13), on the hypothetical assumption that the continuity of flowing medium always takes place in the region under consideration. Thus, if the computed pressure becomes negative at some point, then this value is replaced with small positive value p_ε, $0 \leqslant p_\varepsilon \leqslant 1$ bar. This procedure enables us to apply Eqs. (12)–(14) over the total length of spiral channel with rectangular cross section, including possible cavity regions.

The numerical solution of the system of Eqs. (12)–(17) is carried out with the use of nondimensional values of pressure, density, and velocity, which are related to the dimensional quantities as follows:

$$\bar{p} = \frac{p}{K_{\text{eff}}}, \quad \bar{\rho} = \frac{\rho}{\rho_0}, \quad \bar{w} = \frac{w}{c_0}, \quad \bar{x} = \frac{x}{L}, \quad \bar{t} = \frac{t}{t_{\text{ref}}}. \tag{19}$$

L is here the length of the spiral channel according to (11), and $t_{\text{ref}} = L/c_0$.

Substituting the expressions $p = \bar{p}K_{\text{eff}}$, $\rho = \bar{\rho}\rho_0$, etc., obtained from (19) into the flow equations (12) and (13) we obtain the equations for barotropic fluid flow in the following form:

$$\frac{\partial\bar{\rho}}{\partial\bar{t}} + \frac{\partial\bar{\rho}\bar{w}}{\partial\bar{x}} = 0,$$

$$\frac{\partial\bar{\rho}\bar{w}}{\partial\bar{t}} + \frac{\partial\bar{\rho}\bar{w}^2 + \bar{p}}{\partial\bar{x}} = -\bar{\rho}\,\frac{gL\cos(\alpha)}{v_{\text{ref}}^2} - \bar{\rho}\,\frac{\lambda L}{2D}\,|\bar{w}|\bar{w}. \tag{20}$$

In the nondimensional form, the equation of state (14) takes the form

$$\bar{p} = \ln\bar{\rho}. \tag{21}$$

It may be seen from Eq. (20) that the pressure can become negative in those subregions, in which the density $\rho < \rho_0$.

While describing the difference equations in the subsequent sections, we omit the bars over the nondimensional quantities for the purpose of brevity of notation.

The Riemann invariants corresponding to Eqs. (12)–(14) can be derived from these equations as follows:

$$\frac{\mathrm{d}p}{\mathrm{d}\rho} = \frac{K_{\text{eff}}}{\rho} = c^2 = \frac{\rho_0 c_0^2}{\rho},$$

$$\mathrm{d}w \pm \frac{1}{c\rho}\,\mathrm{d}p = \mathrm{d}w \pm \frac{K_{\text{eff}}}{c}\,\frac{\mathrm{d}\rho}{\rho^2} = d\left(w \pm \frac{\sqrt{K_{\text{eff}}}\,\mathrm{d}\rho}{\rho^{3/2}}\right) = d\left(w \mp \frac{2\sqrt{K_{\text{eff}}}}{\sqrt{\rho}}\right) = d(w \mp 2c). \tag{22}$$

From here the following expressions for the Riemann invariants are obtained:

$v_1 = w + 2\sqrt{K_{\text{eff}}/\rho}$ along the characteristic $\mathrm{d}x/\mathrm{d}t = w - c$,

$v_2 = w - 2\sqrt{K_{\text{eff}}/\rho}$ along the characteristic $\mathrm{d}x/\mathrm{d}t = w + c$.

These formulas will be used for the derivation of the difference boundary conditions at the lower inlet and upper outlet of the spiral channel.

The initial conditions are as follows:

$$\bar{p}(x,0) = 0, \quad \bar{w}(x,0) = \bar{w}_0, \quad \bar{\rho}(x,0) = 1, \tag{23}$$

where $\bar{w}_0$ is the nondimensional fluid velocity, which is obtained from the required volume rate Q_0 and the area of fluid flow cross section $A = B_1/H_1$,

$$\bar{w}_0 = -Q_0/(Ac_0). \tag{24}$$

As the boundary condition at the inlet of the spiral compensator, that is at its lower side in the direction of the percussion–rotary drill, two variants for the pressure function $P_0(t)$ are considered:

1. *Smooth periodic function*

$$p_0(t) = \frac{1}{2}\left[p_{\min} + p_{\max} + (p_{\max} - p_{\min})\sin\left(\bar{\omega}t - \frac{\pi}{2}\right)\right]. \tag{25}$$

2. *Periodic jump function*

$$p_0(t) = \frac{1}{2}\left[p_{\min} + p_{\max} + (p_{\max} - p_{\min})\,\mathrm{sign}\left(\sin\left(\bar{\omega}t - \frac{\pi}{2}\right)\right)\right]. \tag{26}$$

The values of $p_{\min}$ and $p_{\max}$ ($0 < p_{\min} < p_{\max}$), that is the minimum and maximum pressure values at the inlet of spiral channel, depend on the specific type of the percussion–rotary drill (for example,

$p_{\min} = 0.2$ MPa and $p_{\max} = 30$ MPa). In this equation, $\bar{\omega}$ is the angular velocity, $\bar{\omega} = 2\pi f$, and f is the frequency of pressure oscillations (for example, 30 Hz).

The boundary conditions at the upper outlet of the spiral are determined depending on the flow character at that end, as this will be shown in the subsequent sections.

5. Numerical schemes

5.1. The TVD scheme

The fluid dynamics problem under consideration is characterized by the presence of strong discontinuities in the solution. It is, therefore, necessary to interpret the corresponding solution of the governing equations of fluid flow as the generalized solutions (Rožděstvenskii and Yanenko, 1983). It should be noted that there are sufficiently many finite difference methods for the shock-capturing computation of the generalized solutions of hyperbolic systems of conservation laws (see, for example, LeVeque, 1992). Various monotonous and quasi-monotonous schemes having a high order of accuracy in the sense of the Taylor expansion on smooth solutions have gained a widespread acceptance for the solution of such problems. The TVD scheme of Harten (1983), the ENO schemes (Harten and Osher, 1987), the modified Godunov type schemes (Toro, 1999) as well as their different modifications belong to such schemes.

The first TVD schemes proposed by Harten (1983) and Yee et al. (1985) had the second order of accuracy in subregions of smooth flow. A review of higher-order extensions of the TVD scheme may be found in Daiguji et al. (1997).

In this section we describe a second-order variant of the TVD scheme, which is based on the version of this scheme proposed by Yee et al. (1985). Before proceeding to the presentation of the TVD scheme we would like to discuss the following two peculiarities of the dimensionless equations (20) governing the barotropic fluid flow.

The first important peculiarity of system (20) is that it does not become stiff in the case of low Mach number flows. In order to show this let us rewrite the system of equations (20) in vector/matrix form as

$$\frac{\partial U}{\partial t} + \frac{\partial F(U)}{\partial x} = S(U), \tag{27}$$

where

$$U = \begin{pmatrix} \rho \\ q \end{pmatrix}, \quad F(U) = \begin{pmatrix} q \\ p + \rho w^2 \end{pmatrix}. \tag{28}$$

Here $q = \rho w$ and $S(U)$ is the vector of source terms,

$$S(U) = \begin{pmatrix} 0 \\ S_1(U) + S_2(U) \end{pmatrix},$$

$$S_1(U) = -C_1\rho, \quad S_2(U) = -C_2|q|w \tag{29}$$

with

$$C_1 = \frac{gL\cos(\alpha)}{v_{\text{ref}}^2}, \qquad C_2 = \frac{\lambda L}{2D}. \tag{30}$$

The Jacobi matrix $A(U) = \partial F(U)/\partial U$ has the form

$$A(U) = \begin{pmatrix} 0 & 1 \\ c^2 - w^2 & 2w \end{pmatrix}, \tag{31}$$

where c is the sound velocity, $c^2 = 1/\rho$. The eigenvalues λ_1, λ_2 of matrix (31) are as follows:

$$\lambda_1 = w - c, \qquad \lambda_2 = w + c. \tag{32}$$

The condition number $\text{Cond}(A) = \|A\| \cdot \|A^{-1}\|$ may be estimated as follows using the spectral norm of a matrix:

$$\text{Cond}(A) = \frac{\max(|\sigma_1|, |\sigma_2|)}{\min(|\sigma_1|, |\sigma_2|)} = c^2 \left[1 - \frac{2M^2(c^4 - 1 - 4c^2)}{c^4 - 1 - 4c^2M^2}\right]^{1/2} + O(M^3), \tag{33}$$

where σ_1 and σ_2 are the singular numbers of matrix A, and M is the Mach number, $M = |w|/c$. It follows from (33) that the quantity $\text{Cond}(A)$ remains finite as $M \to 0$: $\lim_{M\to 0} \text{Cond}(A) = c^2$. In other words, the system of equations (27), (28) does not become stiff for low Mach number flows.

Despite the fact that the above noted first peculiarity of the system of equations (27), (28) alleviates certain difficulties related to its numerical integration, there is the second peculiarity, which impedes the numerical integration of Eqs. (27), (28). It turns out that the source term $S_2(U)$ in (29) is a stiff source term. According to LeVeque and Yee (1990), a source term is considered to be stiff if the constant factor entering this term is sufficiently large. In the case of actual spiral compensators, the constant coefficient C_2 entering $S_2(U)$ lies in the range $30 < C_2 < 60$. LeVeque and Yee (1990) considered the stiff source terms involving the constant factors lying in the range from 1 to 1000. Therefore, our source term $S_2(U)$ may be considered as a moderately stiff source term.

The second source term $S_1(U)$ in (29) proves to be of the order 10^{-4}, which is very small. This is explained by the fact that the spiral channel of an actual compensator has many turns, so that the neighbouring turns adhere tightly to one another (see Fig. 2). Therefore, the angle α in (30) differs little from $\pi/2$.

It was shown by LeVeque and Yee (1990) that in the case of stiff source terms, a numerical phenomenon of incorrect propagation speeds of discontinuities is observed. In addition, an overshoot may appear in the numerical solution behind the discontinuity front even if a TVD scheme is used. The following measures were proposed by LeVeque and Yee (1990) to resolve these difficulties: (i) the use of implicit approximations for the stiff source terms; (ii) the use of splitting methods, in which one alternates between solving a system of conservation laws, with no source terms, and a system of ordinary differential equations involving the source terms.

We now present a TVD scheme, which we have used for the numerical modelling of barotropic fluid flow in spiral channel. It combines the ideas for the construction of TVD schemes proposed by Yee et al. (1985), Yee and Harten (1987), and Takakura et al. (1989).

We will assume in this section that the values of the numerical solution vector U_j^n are computed at the centres of the cells of an uniform grid in the interval $0 \leqslant x \leqslant 1$, so that

$$U_j^n = U(x_j, t_n), \quad x_j = (j - 0.5)h, \quad j = 1, \ldots, N-1;$$

$h = 1/(N-1)$, $t_n = \tau_0 + \tau_1 + \cdots + \tau_{n-1}$.

The explicit TVD scheme used by us has the form

$$\frac{U_j^{n+1} - U_j^n}{\tau_n} + \frac{\tilde{F}_{j+1/2}^n - \tilde{F}_{j-1/2}^n}{h} = S_j^n, \tag{34}$$

where

$$\tilde{F}_{j+1/2}^n = \frac{1}{2}(F_j^n + F_{j+1}^n) + R_{j+1/2}\varphi_{j+1/2}^n. \tag{35}$$

Here $F_j^n = F(U_j^n)$, $R_{j+1/2} = R(U_{j+1/2})$, and R is the matrix entering the representation $A(U) = R\Lambda R^{-1}$, where $A(U)$ is the Jacobi matrix (31) and

$$R = \begin{pmatrix} 1 & 1 \\ w-c & w+c \end{pmatrix}, \quad \Lambda = \begin{pmatrix} w-c & 0 \\ 0 & w+c \end{pmatrix}, \quad R^{-1} = \begin{pmatrix} \frac{c+w}{2c} & -\frac{1}{2c} \\ \frac{c-w}{2c} & \frac{1}{2c} \end{pmatrix}. \tag{36}$$

The quantity $\varphi_{j+1/2}^n$ entering (35) was computed as follows (Yee and Harten, 1987):

$$\varphi_{j+1/2}^n = \{\varphi_{j+1/2}^{(1)}, \varphi_{j+1/2}^{(1)}\},$$
$$\varphi_{j+1/2}^{(m)} = \tfrac{1}{2}\psi(l_{j+1/2}^{(m)})(\tilde{g}_j^{(m)} + \tilde{g}_{j+1}^{(m)}) - \psi(l_{j+1/2}^{(m)} + \gamma_{j+1/2}^{(m)})\alpha_{j+1/2}^{(m)}, \quad m = 1, 2, \tag{37}$$

where $l_{j+1/2}^{(1)}$ and $l_{j+1/2}^{(2)}$ are the eigenvalues of matrix A (31), that is

$$l_{j+1/2}^{(1)} = w_{j+1/2}^n - c_{j+1/2}^n, \quad l_{j+1/2}^{(2)} = w_{j+1/2}^n + c_{j+1/2}^n,$$

and

$$\psi(z) = Q(z) - \frac{\tau}{h}z^2, \tag{38}$$

$$Q(z) = \begin{cases} \frac{1}{2}(\frac{z^2}{\delta} + \delta), & |z| < \delta, \\ |z|, & |z| \geqslant \delta. \end{cases} \tag{39}$$

The value δ in (39) is a user-specified constant lying in the interval $[0.01, 0.25]$ (Aki, 1989).

It is to be noted that the item $(-\tau/h)z^2$ introduced into expression (38) for $\psi(z)$ ensures the second order of accuracy of scheme (34) in time in subregions of smooth flow (LeVeque, 1992).

The values $\alpha_{j+1/2}^{(m)}$ and $\gamma_{j+1/2}^{(m)}$ entering (37) are computed as follows:

$$\alpha_{j+1/2} = \{\alpha_{j+1/2}^{(1)}, \alpha_{j+1/2}^{(2)}\}, \quad \alpha_{j+1/2} = R_{j+1/2}^{-1}(U_{j+1}^n - U_j^n), \quad m = 1, 2;$$

$$\gamma_{j+1/2}^{(m)} = \begin{cases} \frac{1}{2}\psi(l_{j+1/2}^{(m)})(g_{j+1}^{(m)} - g_j^{(m)})/\alpha_{j+1/2}^{(m)}, & \alpha_{j+1/2}^{(m)} \neq 0, \\ 0, & \alpha_{j+1/2}^{(m)} = 0. \end{cases}$$

The values of $U_{j+1/2}^n$ entering the expressions for $R_{j+1/2}$, $l_{j+1/2}^{(m)}$, and $R_{j+1/2}^{-1}$ were computed as the arithmetic means, that is $U_{j+1/2}^n = 0.5(U_j^n + U_{j+1}^n)$.

To enhance the resolution of shock wave fronts we computed the values $\tilde{g}_j^{(m)}$ entering (37) by formulas (Yee et al., 1985)

$$\tilde{g}_j^{(m)} = (1 + \omega^{(m)}\theta_j^{(m)})g_j^{(m)}, \quad m = 1, 2. \tag{40}$$

The quantity $g_j^{(m)}$ in (40) is called the flux limiter. Arora and Roe (1997) have formulated the general requirements for the flux limiter functions. Many flux limiters were proposed in the literature until now. Some of them were listed, for example, by Aki (1989) and Yee et al. (1999). As was noted by Yee et al. (1999), the choice of an optimal flux limiter is problem dependent.

In order to find an optimal flux limiter for the problem of one-dimensional barotropic fluid flow we have tried the following three flux limiters:

1. The flux limiter of Yee and Harten (1987):

$$g_j^{(m)} = S\max[0, \min(|\alpha_{j+1/2}^{(m)}|, S\alpha_{j-1/2}^{(m)})], \quad S = \operatorname{sign}(\alpha_{j+1/2}^{(m)}). \tag{41}$$

2. The flux limiter of van Leer (Van Leer, 1979; LeVeque, 1992):

$$g_j^{(m)} = \frac{\hat{\theta}_j^{(m)} + |\hat{\theta}_j^{(m)}|}{1 + \hat{\theta}_j^{(m)}},$$

where

$$\hat{\theta}_j^{(m)} = \frac{\Delta_{j+1/2}U_j^{(m)}}{\Delta_{j-1/2}U_j^{(m)}}, \qquad \Delta_{j+1/2}U_j^{(m)} = U_{j+1}^{(m)} - U_j^{(m)}.$$

Here $U_j^{(1)} = \rho_j^n$, $U_j^{(2)} = q_j^n = \rho_j^n w_j^n$.

3. The flux limiter from the works of Aki (1989) and Yee et al. (1999):

$$g_j^{(m)} = M[2\alpha_{j+1/2}^{(m)}, 2\alpha_{j-1/2}^{(m)}, \frac{1}{2}(\alpha_{j+1/2}^{(m)} + \alpha_{j-1/2}^{(m)})],$$

where the symbol M denotes conventional minmod operation defined as

$$M(x, y, \ldots) = \begin{cases} S\min(|x|, |y|, \ldots) & \text{if } \operatorname{sgn}(x) = \operatorname{sgn}(y) = \cdots = S, \\ 0 & \text{otherwise.} \end{cases}$$

As our test computations have shown, the well-known flux limiter of Harten (41) leads to the most reliable and stable numerical algorithm. Therefore, all the computational results presented in Section 6 have been obtained with the use of the flux limiter (41).

For the quantity $\theta_j^{(m)}$ in (40) we have used the formula from Takakura et al. (1989):

$$\theta_j^{(m)} = \frac{|\Delta_{j+1/2} U_j^{(m)} - \Delta_{j-1/2} U_j^{(m)}|}{|\Delta_{j+1/2} U_j^{(m)}| + |\Delta_{j-1/2} U_j^{(m)}|}, \quad m = 1, 2. \tag{42}$$

The user-specified constants $\omega^{(m)}$ in (40) can be different from one characteristic field to another. Yee et al. (1985) have considered the values $\omega^{(m)} = 1$ and $\omega^{(m)} = 2$.

Note that Yee et al. (1985) have proposed the formula

$$\theta_j^{(m)} = \frac{|\alpha_{j+1/2}^{(m)} - \alpha_{j-1/2}^{(m)}|}{|\alpha_{j+1/2}^{(m)}| + |\alpha_{j-1/2}^{(m)}|}, \quad m = 1, 2.$$

But our calculations of fluid flows in spiral compensators have shown that the use of (42) leads to a more reliable computer code.

For the approximation of the source term S_j^n in (34) we have used a simple one-point formula:

$$S_j^n = \begin{pmatrix} 0 \\ -C_1 \rho_j^n - C_2 |q_j^n| w_j^n \end{pmatrix}.$$

For the computation of the flux vector $F(U)$ on the left boundary $x = 0$, the values of $\rho_{1/2}^n$ and $w_{1/2}^n$ are needed on this boundary. We have implemented a procedure similar to the one described by Jameson et al. (1981). First of all we note that the fluid pressure $p_0(t)$ on the left boundary is known from the boundary condition (25) or (26). This enables us to find the density value: $\rho_{1/2}^n = \exp(p_0(t_n))$. We now use the Riemann invariant v_1 to compute the velocity value $w_{1/2}^n$: $v_1^n = w_1^n + 2c_1^n$. Since this invariant is conserved along the characteristic $\mathrm{d}x/\mathrm{d}t = w - c$, we can write approximately that $w_{1/2}^n + 2c_{1/2}^n = v_1^n$. Since $c_{1/2}^n = \sqrt{1/\rho_{1/2}^n}$, we can find the velocity value for $x = 0$: $w_{1/2}^n = v_1^n - 2\sqrt{1/\rho_{1/2}^n}$.

A similar procedure was implemented on the right boundary $x = 1$ with regard to the fact that the fluid flow is always subsonic at this boundary of the spiral compensator. Let us at first compute both the Riemann invariants v_1 and v_2:

$$v_1 = v_{1,N-1}^n = w_{N-1}^n - 2c_{N-1}^n, \quad v_2^0 = w_0 + 2c^0 = w_0 + 2.0,$$

where w_0 is the fluid velocity taken from the initial condition (23). That is we take the value of w_0, which corresponds to the given volume rate of fluid supplied "at infinity" by the pump located on the ground surface, see also (24). Then on the right boundary $x = 1$ we obtain the needed values $\rho_{N-1/2}^n$ and $w_{N-1/2}^n$ as follows:

$$w_{N-1/2}^n = \frac{1}{2}(v_{1,N-1}^n + v_2^0), \quad \rho_{N-1/2}^n = \left(\frac{1}{c_{N-1/2}^n}\right)^2 = \left[\frac{1}{\frac{1}{4}(v_2^0 - v_{1,N-1}^n)}\right]^2.$$

The time step τ_n was computed as follows:

$$\tau_n = \min_j \frac{Ch}{|w_j^n| + c_j^n}. \tag{43}$$

Fig. 4. Computational grid.

The value c_j^n is here the sound velocity, $c_j^n = \sqrt{1/\rho_j^n}$, and C is the Courant number, which must lie in the interval $0 < C < 1$ to ensure stability of numerical computations.

5.2. Splitting in terms of physical processes

In this section, we consider one more difference scheme for the numerical integration of flow equations (20). This scheme is similar to an explicit–implicit scheme of splitting in terms of physical processes, which was proposed by Ostapenko (1997) for the numerical integration of the system of the Saint-Venant shallow water equations, which is mathematically sufficiently close to the fluid dynamic system, which is solved in the present work. This is a simple finite difference first-order method with linear artificial viscosity for the numerical solution of differential equations presented in Section 4. A similar numerical method was used successfully by Ostapenko (1999) for numerical solution of a two-dimensional two-layer shallow water problem.

We now present the difference equations of the scheme of Ostapenko (1999) as applied to the flow equations (20). At first we define in the interval $0 \leqslant \bar{x} \leqslant 1$ a uniform grid with the nodes

$$\bar{x}_j = (j-1)h, \quad j = 1, \ldots, N, \tag{44}$$

where N is the number of grid nodes and h is the step size, $h = 1/(N-1)$. The velocity values w_j and mass flux values $q_j = (\rho w)_j$ are computed in the above grid nodes, whereas the density values $\rho_{j+1/2}$ are computed in the middle of the intervals $[x_j, x_{j+1}]$ (Fig. 4).

The difference scheme for the continuity equation (12) has the following form under the above conventions:

$$\frac{\rho_{j+1/2}^{n+1} - \rho_{j+1/2}^n}{\tau_n} + \frac{q_{j+1}^n - q_j^n}{h} = 0, \quad n = 0, 1, 2, \ldots, \ j = 1, 2, \ldots, N-1. \tag{45}$$

The quantity τ_n is here the time step of the finite difference method, $\rho_{j+1/2}^n = \rho(\bar{x}_{j+1/2}, t_n)$, with $t_n = \tau_0 + \tau_1 + \cdots \tau_{n-1}$, and $\bar{x}_{j+1/2} = (j-1/2)h$, $q_j^n = q(\bar{x}_j, t_n)$. The density ρ is computed for each time step $t = t_{n+1}$ $(n = 0, 1, 2, \ldots)$. Eq. (21) is used to compute the corresponding pressure values:

$$p_{j+1/2}^{n+1} = \ln \rho_{j+1/2}^{n+1}, \quad j = 1, 2, \ldots, N-1. \tag{46}$$

The momentum equation (13) is approximated by using the splitting in terms of physical processes (Ostapenko, 1999). At the first stage, only the pressure term, the convection term, and the gravity force are taken into account. The losses due to wall friction are not considered:

$$\frac{q_j^* - q_j^n}{\tau_n} + \frac{q_{j+1}^n w_{j+1}^n - q_{j-1}^n w_{j-1}^n}{2h} + \frac{p_{j+1/2}^{n+1} - p_{j-1/2}^{n+1}}{h} = -C_1 \rho_j^{n+1} + W_j^n. \tag{47}$$

In this equation,

$$\rho_j^{n+1} = (1/2)(\rho_{j-1/2}^{n+1} + \rho_{j+1/2}^{n+1}), \tag{48}$$

and W_j^n is the so-called artificial viscosity, whose differential form is as follows:

$$W = \kappa_1 h(|w|q_x)_x + \kappa_2 h q_{xx}. \tag{49}$$

The artificial viscosity is introduced for the purpose of damping the parasitic oscillations of numerical solution in the neighbourhood of shock waves. κ_1 and κ_2 are the constant and positive coefficients, which are determined with the aid of test computations of problems involving stationary shock waves. These coefficients must ensure a monotone localization of shock wave fronts at the minimal oscillations (Ostapenko, 1999). The conducted tests gave for the task considered in this work the values $\kappa_1 \approx 0.8$ and $\kappa_2 \approx 0.15$. The second term ($\kappa_2 h q_{xx}$) for the definition of the artificial viscosity was added for the reason that the fluid inflow due to water shock reduces the value of $|w|$ so significantly that the first term ($\kappa_1 h(|w|q_x)_x$) becomes insufficiently efficient.

The approximation of Eq. (49) is as follows:

$$W_j^n = \kappa_1 h \frac{|w_{j+1/2}^n|(q_{j+1}^n - q_j^n) - |w_{j-1/2}^n|(q_j^n - q_{j-1}^n)}{h^2} + \kappa_2 h \frac{q_{j+1}^n - 2q_j^n + q_{j-1}^n}{h^2}. \tag{50}$$

At the second stage, the effect of wall friction is taken into account by using the following implicit approximation:

$$\frac{q_j^{n+1} - q_j^*}{\tau_n} = -\rho_j^{n+1} C_2 |w_j^n| \frac{q_j^{n+1}}{\rho_j^{n+1}}, \tag{51}$$

where the constant coefficient C_2 is given by the second equation in (30). It follows from here that

$$q_j^{n+1} = q_j^* \left(1 + \tau_n C_2 |w_j^n|\right)^{-1}. \tag{52}$$

Such an implicit approximation of wall friction in a channel ensures a stable numerical algorithm.

After the computation of q_j^{n+1}, w_j^{n+1} is determined from the equation

$$w_j^{n+1} = 2q_j^{n+1}/(\rho_{j-1/2}^{n+1} + \rho_{j+1/2}^{n+1}). \tag{53}$$

Without the artificial viscosity ($\kappa_1 = \kappa_2 = 0$) the finite difference method has second order in space and first order in time, that is the error of this method lies in the order of smallness of $O(\tau_n) + O(h^2)$. The introduction of artificial viscosity, an indispensable tool for ensuring a stable numerical algorithm at the computation of strong shock waves, leads to the reduction of the spatial accuracy to the first order.

Basing on the physical analogy with the Navier–Stokes equations the artificial viscosity is introduced only into the momentum equation. The spatial approximation of the continuity equation then has the second order also when the artificial viscosity is introduced.

We now present the difference boundary condition at the left end $x = 0$ of the spatial integration interval. As in the case of the TVD scheme, the density value ρ_1^{n+1} is found from the boundary condition (25) or (26) for fluid pressure: $\rho_1^{n+1} = \exp(p_0(t_{n+1}))$. Then the mass flow rate q_1^{n+1} at point $x = 0$ is computed by using the one-sided differences:

$$q_1^* = q_1^n - \frac{\tau}{h}(q_2^n w_2^n - q_1^n w_1^n) - \frac{2\tau}{h}(p_{3/2}^{n+1} - p_1^{n+1}) - \tau_n C_1 \rho_1^{n+1},$$

$$q_1^{n+1} = q_1^*/(1 + \tau_n C_2 |w_1^n|), \quad w_1^{n+1} = q_1^{n+1}/\rho_1^{n+1}.$$

For the definition of boundary conditions at the outlet of spiral (at $x = L$) the following two cases are considered:

1. The flow is in subcritical range, i.e., $|w| < c$. Let us at first denote by v_1^0 the initial value of the Riemann invariant v_1 under the conditions $w = w_0$ and $c = c_0$, i.e. $v_1^0 = w_0 + 2c_0$. In addition, it is assumed that the conditions at $x = +\infty$ are translated along the characteristic $\mathrm{d}x/\mathrm{d}t = w - c$ at point $x = L$ for $t \geqslant 0$. In this case, the following relation is valid for $x = x_N = L$:

$$w_N^{n+1} + 2c_N^{n+1} = v_1^0. \tag{54}$$

With regard for the above-described splitting in terms of physical processes, the values of q_N^{n+1} and ρ_n^{n+1} can be computed with the aid of (54) from the following equations:

$$\frac{q_N^* - q_N^n}{\tau_n} + \frac{q_N^n w_N^n - q_{N-1}^n w_{N-1}^n}{h} + \frac{p_N^n - p_{N-1/2}^n}{h/2} = -C_1 \rho_N^n, \tag{55}$$

$$q_N^{n+1} = q_N^*/(1 + \tau_n C_2 |w_N^{n+1}|) = b. \tag{56}$$

Multiplying Eq. (54) with ρ_N^{n+1} we obtain

$$q_N^{n+1} + 2\rho_N^{n+1} c_N^{n+1} = v_1^0 \rho_N^{n+1}. \tag{57}$$

Substituting q_N^{n+1} from (56) into (57) and assuming $\xi = \sqrt{\rho_N^{n+1}}$ we obtain from (57) the following quadratic equation:

$$b + 2\xi = v_1^0 \xi^2, \quad \text{or} \quad v_1^0 \xi^2 - 2\xi - b = 0, \tag{58}$$

with positive solution

$$\rho_N^{n+1} = (1 + \sqrt{v_1^0 b})^2/((v_1^0)^2). \tag{59}$$

For the case in which the velocity at $x = L$ is constant the following equality obviously holds:

$$\bar{w}_N^{n+1} = -Q_0/(Ac_0). \tag{60}$$

The value of q_N^{n+1} is determined from Eqs. (55) and (56). Since the velocity $\bar{w}_N^{n+1}$ is known in accordance with formula (60), the density ρ_N^{n+1} can be computed immediately from the relation $\rho_N^{n+1} = q_N^{n+1}/w_N^{n+1}$.

2. The flow lies in supercritical range, i.e., $|w| > c$. Since this case is not encountered in the task of numerical modelling of flow in spiral compensators, we will not present here the corresponding difference equations for the right end $i = N$ for the purpose of brevity. We only note that a stable variant of these equations can be obtained by replacing the central differences in the above difference equations (45) and (47) with the backward differences to approximate the derivatives with respect to x in the governing flow equations.

6. Results

6.1. Program test

To validate the developed computer code we have compared the numerical results with the exact analytic solution for the case of the propagation of a stationary shock wave in a channel. The exact solution may be obtained from the following Rankine–Hugoniot relations:

$$u(\rho_1 - \rho_0) = q_1 - q_0, \quad q_1(u - w_1) - q_0(u - w_0) = p_1 - p_0. \tag{61}$$

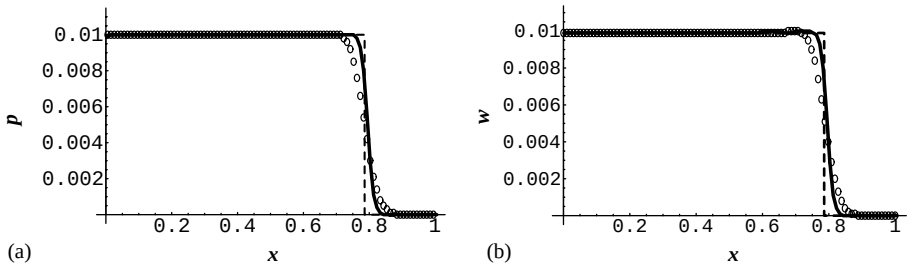

Fig. 5. Stationary shock wave in channel in the absence of source terms in (27) at $t = 0.746$: (a) pressure and (b) velocity of the fluid. ($\circ\circ\circ$) the scheme of Ostapenko; (—) the TVD scheme; (- - -) exact solution.

In these equations, u is the stationary velocity of shock wave. The quantities with subscript "1" refer to the fluid state behind the shock wave front, and the quantities with subscript "0" refer to the state ahead of shock wave front. We consider the case in which the medium ahead of shock wave is at rest, i.e., $w_0 = q_0 = 0$. It then follows from (61) that

$$u(\rho_1 - \rho_0) = q_1, \qquad uq_1 = q_1 w_1 + p_1 - p_0. \tag{62}$$

The multiplication of both sides of the first equation in (62) by u implies

$$u^2(\rho_1 - \rho_0) = uq_1. \tag{63}$$

Since in addition $w_1 = q_1/\rho_1$ and, thus, $q_1 w_1 = q_1^2/\rho_1 = u^2(\rho_1 - \rho_0)^2/\rho_1$, the second equation of (62) may also be rewritten as

$$u^2(\rho_1 - \rho_0) = u^2(\rho_1 - \rho_0)^2/\rho_1 + p_1 - p_0. \tag{64}$$

Formulas (63) and (64) yield the following formula for the squared shock wave velocity:

$$u^2 = (\rho_1/\rho_0)[\ln(\rho_1) - \ln(\rho_0)]/(\rho_1 - \rho_0). \tag{65}$$

If the values ρ_0 and ρ_1 are given, then one can compute with the aid of (65) the velocity of stationary shock wave, and the formula

$$w_1 = u(\rho_1 - \rho_0)/\rho_1 \tag{66}$$

and (21) yield also the values of the velocity and pressure behind its front.

Since the strength of shock waves in spiral compensators is relatively weak we have taken approximately the same value of the dimensionless fluid density ρ_1 as in the case of fluid flows in spiral compensators: $\rho_1 = 1.01$, $\rho_0 = 1.0$. We have considered two cases:

(a) there are no source terms in the governing equations (27), (28), that is $C_1 = 0$, $C_2 = 0$ in (29);
(b) there are nonzero source terms whose coefficients have approximately the same magnitude as in spiral compensators; we have used the values $C_1 = 0.001$ and $C_2 = 50.0$ in (29).

Fig. 5 shows the computational results for the case of the absence of source terms in flow equations (27). Then the exact solution (65), (66) and (21) is exactly applicable.

In the case of the TVD scheme we have used the values: $C = 0.25$ in (43), $\omega^{(1)} = 0.5$, $\omega^{(2)} = 0.5$ in (40), $\delta = 0.125$ in (39).

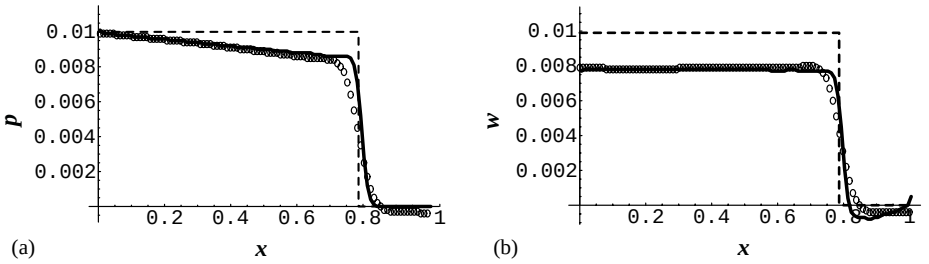

Fig. 6. Stationary shock wave in channel in the presence of source terms in (27) at $t = 0.746$: (a) pressure and (b) velocity. ($\circ\circ\circ$) the scheme of Ostapenko; (—) the TVD scheme; (- - -) exact solution for the case of the absence of source terms in (27).

In the case of the scheme of Ostapenko, $C = 0.5$ in (43), $\kappa_1 = 1.0$, $\kappa_2 = 0.15$ in (50). The number of grid nodes $N = 101$ for both the finite-difference methods. It can be seen from Fig. 5 that the TVD scheme ensures monotone numerical solution profiles, which are steeper in the region of the smeared shock wave front than in the case of the Ostapenko's scheme (45)–(52).

It may be seen from Fig. 6 that the exact shock wave speed is reproduced correctly by both the TVD scheme and the Ostapenko's scheme despite the presence of a moderately stiff source term in the momentum equation. The presence of source terms (29) with $C_1 = 0.001$ and $C_2 = 50.0$ leads to the reduction of the pressure and velocity values behind the shock wave front as the time t (and the distance propagated by the shock wave) increases.

6.2. Numerical modelling of real flow processes

After a successful test the code can be used for the investigation of real flow processes in the spiral channel with rectangular cross section in Fig. 7.

The purpose of these studies is finally the determination of such geometric parameters of the spiral, which ensure the maximum damping effect for the periodic shock waves propagating from bottom to top.

The following assumptions are made for the solution of this task:

1. The time interval $[0, t_{\max}]$ for the solution of Eqs. (12)–(14) is chosen in such a way that many shock waves propagate along the spiral channel. The resulting number of time steps then has, at a Courant number $C = 0.5$, the order of magnitude of 8000.
2. The geometry of the spiral channel with rectangular cross section is according to (2), (5), and (7) a function of the parameters

$$a, B, H, d, z_{\max}, \psi_1. \tag{67}$$

Let us denote by p_{out} the maximum fluid pressure at the upper outlet of the spiral compensator. The computations clearly show that this pressure value depends strongly on the fluid volume rate Q_0. With regard to the desired damping effect, i.e., the reduction of the inlet pressure oscillating between $p_{\min}$ and $p_{\max}$ to the maximum outlet pressure p_{out}, which depends both on Q_0 and

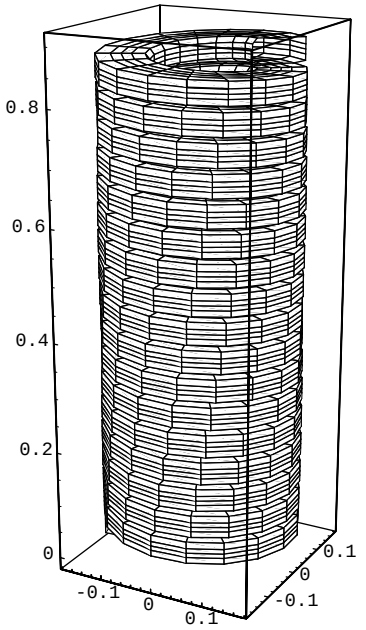

Fig. 7. Model of spiral channel.

the elasticity modules E_F and E_M, the following function may be obtained from (67) for the determination of p_{out}:

$$p_{out} = F(a, B, H, d, z_{max}, \psi_1, p_{min}, p_{max}, Q_0, E_F, E_M). \tag{68}$$

3. Large computer expenses resulting from (68) can be reduced very significantly by the specification of the following parameters:

$E_F = 20.5 \times 10^8$ N/m^2; $E_M = 200 \times 10^9$ N/m^2;

$d = 1$ cm; $z_{max} = 0.9$ m;

$a = 13$ cm; $\psi_1 = 0.99$;

1 MPa $\leqslant p_0(t) \leqslant$ 16 MPa; $\rho_0 = 1100$ kg/m^3.

As a result, function (68) reduces to

$$p_{out} = F(B, H, Q_0). \tag{69}$$

The following tables present the computed results for the case of a periodic pressure jump function 1 MPa $\leqslant p_0(t) \leqslant$ 16 MPa (Fig. 8(a)) with the frequency 25 Hz versus the arguments of function (69). In practical calculations, the value of p_{out} was found at the last time step as the pressure value at the first local maximum nearest to the upper end in the pressure profile $p(x, t)$.

Since the above-described TVD scheme contains a number of user-specified parameters it was important to find those values of these parameters, which ensure the monotone numerical solution with steep profiles in the zones of smeared shock waves. For definiteness we have taken the case

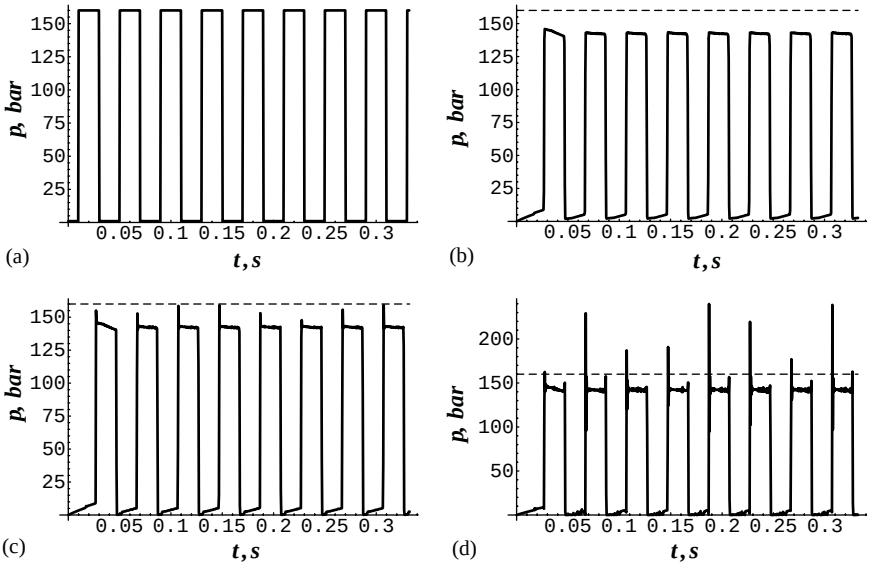

Fig. 8. The pressure distributions: (a) the pressure $p_0(t)$ at the spiral inlet as a function of time; (b)–(d) the numerical solution for the pressure at the spiral outlet $x = 1$ as function of time: (b) $\omega^{(1)} = 1,\ \omega^{(2)} = 0.5$; (c) $\omega^{(1)} = 1,\ \omega^{(2)} = 1.0$; (d) $\omega^{(1)} = 1,\ \omega^{(2)} = 1.5$.

considered below in the extreme right column of Table 2: the volume rate Q_0=600 l/min., B=0.09 m, $H = 0.0428$ m. For the series of runs presented in Fig. 8, a discontinuous pressure curve (26) was used at the spiral inlet $x = 0$. It was found by numerical experiments that the constant δ in (39) can be taken in the interval $0.1 \leqslant \delta \leqslant 0.15$. The results presented in Figs. 8(b)–(d) were obtained with $\delta = 0.125$. The dashed line shows in these figures the maximum value $p_{\max} = 160$ bar in the left boundary condition (26) for the pressure.

The number of the executed time steps in all runs presented in Fig. 8 is the same: $n = 16\,000$, the Courant number $C = 0.25$ in (43). The number of grid nodes $N = 201$ for all runs.

The purpose of the runs presented in Figs. 8(b)–(d) was the determination of optimal parameters $\omega^{(1)}$ and $\omega^{(2)}$ in (40). As can be seen from Fig. 8, the optimal combination of $\omega^{(1)}$ and $\omega^{(2)}$ is as follows: $\omega^{(1)} = 1.0$, $\omega^{(2)} = 0.5$. One can, of course, also take the values of $\omega^{(2)}$ in the interval $0 \leqslant \omega^{(2)} < 0.5$, but the width of the zone of smearing of shock waves becomes larger as $\omega^{(2)}$ reduces. With an increase in $\omega^{(2)}$, so that $\omega^{(2)} > 0.5$, the overshoots appear in the profile of $p(1, t)$, and their amplitude increases with $\omega^{(2)}$. We can explain this phenomenon qualitatively as follows. When larger values of $\omega^{(2)}$ are taken, the TVD scheme becomes less dissipative in the regions of smeared shock wave fronts (the profiles become steeper in these zones). As a result, the numerical dissipation becomes insufficient to suppress the stiffness of the moderately stiff source term $S_2(U)$ in (29), and this leads to the appearance of overshoots in the numerical solution profiles.

As was mentioned in Section 5 under the choice of the function $\psi(z)$ in form (38) the TVD scheme (34)–(42) has the second order of accuracy both in space and time in the subregions of smooth flow. This form of $\psi(z)$ was used for the runs of Fig. 8. It was interesting to elucidate the

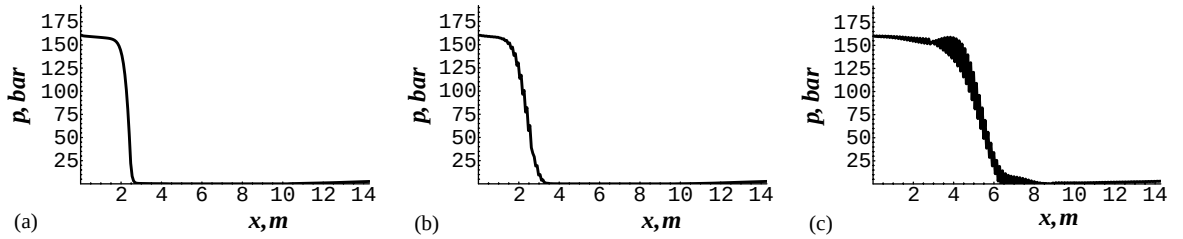

Fig. 9. The pressure distributions along the spiral channel obtained with the aid of the TVD scheme at $\omega^{(1)} = 1$, $\omega^{(2)} = 0$: (a) $C = 0.25$, $n = 16\,000$; (b) $C = 0.50$, $n = 8000$; (c) $C = 0.506$, $n = 8000$.

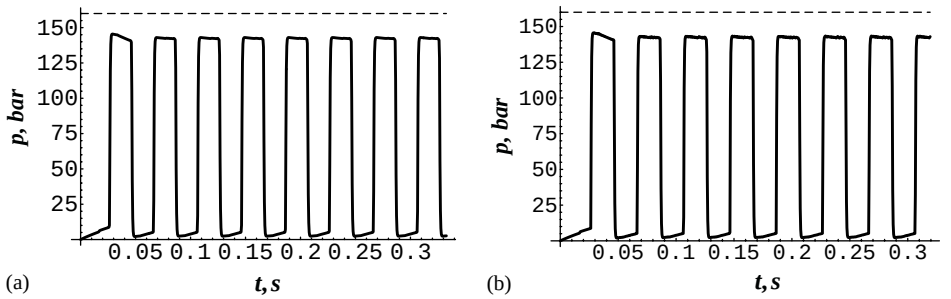

Fig. 10. The pressure distributions versus time at the spiral outlet computed by the TVD scheme at $\omega^{(1)} = 1$, $\omega^{(2)} = 0$: (a) $C = 0.25$, $n = 16\,000$; (b) $C = 0.50$, $n = 8000$.

effect of using $\psi(z)$ in the following form:

$$\psi(z) = Q(z). \tag{70}$$

Then the TVD scheme becomes first-order accurate in time. The runs presented in Figs. 9 and 10 differ from those of Fig. 8 mainly by the use of (70) instead of (38). It can be seen from Fig. 10 that the numerical solution becomes nonmonotonic at $C = 0.5$; at larger values of C the amplitude of numerical oscillations increases nonlinearly with C, so that the TVD scheme becomes unstable for $C = 0.6$.

It may be seen from Fig. 9 that the smearing of shock wave fronts becomes more intense as the value of C increases. This may be explained by the fact that since the time step τ increases with the Courant number, the size of the approximation error of the order $O(\tau)$ also increases linearly with τ. However, even at small values of the Courant number the smearing of shock wave fronts is more intense than in the case of using the function $\psi(z)$ (38), cf. Fig. 11(a). Under the optimal values $\omega^{(1)} = 1.0$, $\omega^{(2)} = 0.5$ the TVD scheme presented in Section 5 remains stable for $0 < C \leqslant 0.33$ in (43). The numerical results presented below in Tables 1–4 were obtained with $C = 0.25$ and the function $\psi(z)$ (38). In Figs. 11 and 12 we present the comparison of the computational results obtained by the TVD scheme (solid lines) and the scheme of Ostapenko (dashed and dotted curves). In the case of the Ostapenko's scheme, the Courant number C was taken to be equal to 0.5 and, thus, only 8000 time steps were needed to achieve the same moment of time as in the case of the TVD scheme. The Riemann invariant $v_1 = v_1^0$

Table 1
The values of the pressure p_{out} at the upper outlet of spiral compensator for $Q_0 = 1000$ l/min, $A = B_1H_1 = 12$ cm^2

B, m	0.04	0.044	0.05	0.06	0.07	0.08
H, m	0.08	0.07	0.06	0.05	0.044	0.04
p_{out}(TVD), bar	172.46	174.49	176.09	178.40	177.33	173.09
p_{out}(Ost.), bar	173.16	175.45	177.22	178.54	175.77	171.65

Table 2
The values of the pressure p_{out} at the upper outlet of spiral compensator for $Q_0 = 600$ l/min, $A = B_1H_1 = 16$ cm^2

B, m	0.0466	0.052	0.06	0.07	0.08	0.09
H, m	0.08	0.07	0.06	0.052	0.0466	0.0428
p_{out}(TVD), bar	157.18	159.23	160.13	158.84	153.25	143.26
p_{out}(Ost.), bar	156.60	158.81	159.61	159.27	152.55	142.30

Table 3
The values of the pressure p_{out} at the upper outlet of spiral compensator for $Q_0 = 300$ l/min, $A = B_1H_1 = 24$ cm^2

B, m	0.05428	0.06	0.07	0.08	0.09	0.10
H, m	0.09	0.08	0.068	0.06	0.05428	0.05
p_{out}(TVD), bar	155.52	151.13	151.63	152.74	144.20	131.43
p_{out}(Ost.), bar	154.08	147.40	147.98	156.29	147.52	131.42

Table 4
The damping effect versus the volume rate Q_0, $B/H = 1$, $B = 0.06$ m

Q_0 l/min	300	400	500	600	700	800	900	1000	1100	1200
p_{out}, bar	156.2	156.9	157.6	159.6	161.5	163.5	165.4	167.3	169.1	170.9
p_{out}, bar	150.9	153.0	154.8	156.5	158.0	151.3	160.5	161.5	162.3	163.1

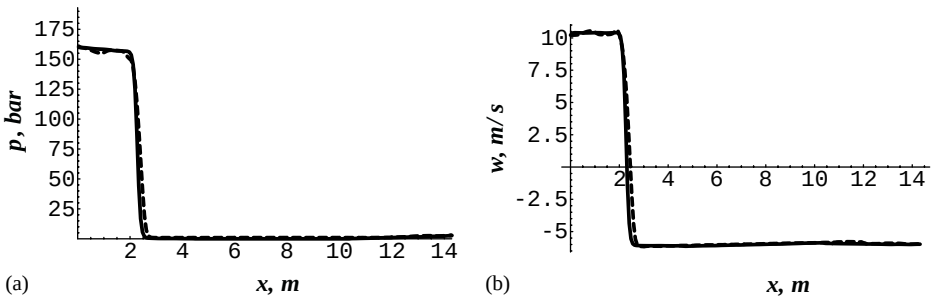

Fig. 11. Computed results for the pressure and velocity along the spiral channel for the moment of time $t = 0.3327$ s.

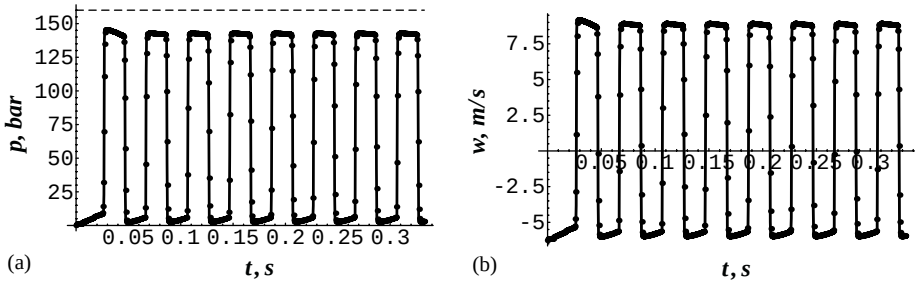

Fig. 12. Computed results for the pressure and velocity at the spiral outlet versus time.

was used here as the right (upper) boundary condition. Fig. 12 confirms the damping effect of spiral.

It can be seen from Fig. 11 and especially Fig. 12 that the results obtained by both the finite difference methods are very close to each other. Both methods produce the same fine details of the temporal behaviour of fluid pressure and velocity at the upper outlet of the spiral compensator despite the fact that the TVD scheme and the difference scheme of Ostapenko are very different in their structure. However, the TVD scheme requires a much larger CPU time to execute the same number of time steps on the same spatial grid: it requires the CPU time, which is by a factor of about 4.66 larger than in the case of the Ostapenko's scheme. Taking into account the fact that in the case of the TVD scheme we had to restrict the Courant number by the value 0.25, the TVD scheme requires a double number of time steps to achieve the same moment of time as in the case of the Ostapenko's scheme (which produces acceptable results for $C \leqslant 0.8$). With regard to this constraint for the Courant number, the above-described TVD scheme is computationally more expensive than the scheme of Ostapenko by a factor of about 9.32. Thus, the scheme of Ostapenko is undoubtedly more advantageous, in terms of needed CPU time, than the above-presented TVD scheme for the numerical modelling of flow processes in spiral compensators.

The symbols p_{out}(TVD) and p_{out}(Ost.) in Tables 1–3 denote the values of the maximum pressure p_{out} at the upper outlet of the spiral compensator, which were obtained by the TVD scheme and the scheme of Ostapenko, respectively.

It may be seen from Table 1 that at a volume rate $Q_0 = 1000$ l/min and free flow cross section $A = 12$ cm^2, the damping effect obviously does not take place. At a volume rate $Q_0 = 600$ l/min and free flow cross section $A = 16$ cm^2, a little damping effect appears, see Table 2.

At a volume rate $Q_0 = 300$ l/min and free flow cross section $A = 24$ cm^2, a significant damping effect is seen (Table 3).

Table 4 illustrates the effect of the volume rate Q_0 on the damping effect for the case of a square cross section ($B = H = 6$ cm), i.e., $B/H = 1$. It may be seen that the pressure reduction at the outlet takes place only at the volume rate $Q_0 \leqslant 600$ l/min. The disappearance of the damping effect at a further increase in volume rate agrees with Eq. (24), which shows that the velocity $\bar{w}_0$ also increases, i.e., the pressure head $(1/2)\rho_0 w_0^2$ also increases. When the shock wave propagating upwards encounters the fluid flowing downwards this results, at a sufficiently high pressure head, in an increase in the shock strength, the effect, which is well known both in theoretical and applied

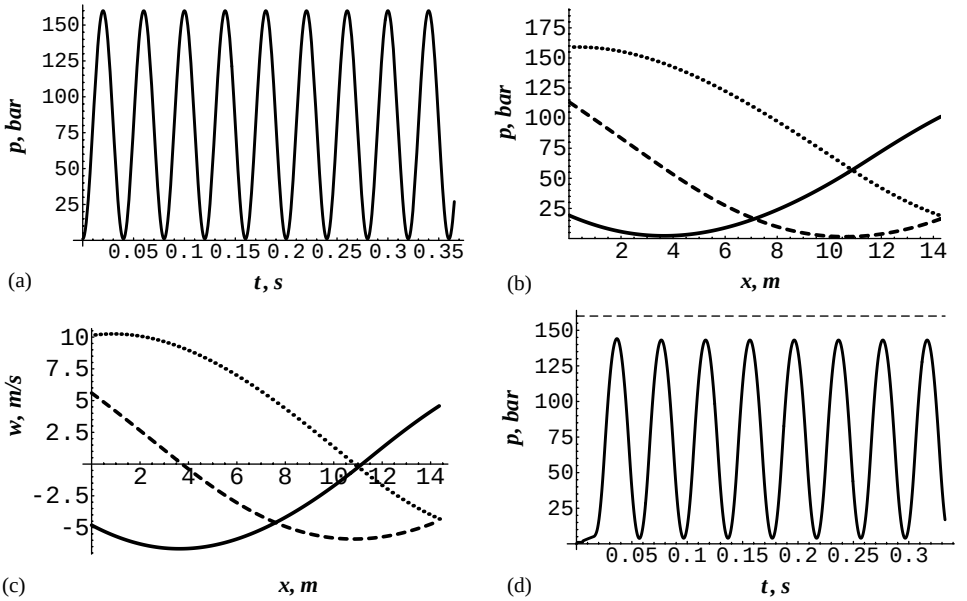

Fig. 13. Computed results for the pressure and velocity in the case of $Q_0 = 600$ l/min: (a) the temporal pressure distribution according to the left boundary condition (25); (b), (c) the pressure and velocity distributions along the spiral channel computed by the TVD scheme and Ostapenko's scheme for different moments of time: (—) $t = 0.3244$ s; (- - -) $t = 0.3327$ s; (· · ·) $t = 0.3410$ s; (d) the fluid pressure as a function of time at the spiral outlet computed by the TVD scheme and Ostapenko's scheme.

fluid dynamics (Roždestvenskii and Yanenko, 1983). At smaller pressure heads, the shock wave strength is damped by fluid friction at the wall as well as by gravity force in the spiral channel.

In the case of a smooth pressure curve (25) at the spiral inlet (see Fig. 13(a)), the maximum pressures at the outlet of spiral are obtained, which are presented in the last row of Table 4 versus the volume rate Q_0. The damping effect is still present even at a volume rate of 800 l/min.

In Fig. 13 we present some computational results obtained in the case of $Q_0 = 600$ l/min and a smooth pressure function (25) at the spiral inlet. In this case, the numerical solutions obtained by the TVD scheme and Ostapenko's scheme coincide within the graphical accuracy. It can be seen from Figs. 13(b) and (c) that in the case of a smooth boundary condition (25), the fluid flow in the spiral compensator represents a sequence of alternating compression and rarefaction zones. Thus, there are no shock waves, in contrast to the case of using a discontinuous pressure function (26). Such a flow regime would be more desirable for the operation of the spiral compensator to improve its wear resistance and to prolong its working life.

We have also investigated the variant of the boundary condition, in which the discontinuous pressure curve was used at the inlet (Fig. 8(a)) together with a user specified fixed volume rate $Q_0 = 600$ l/min. The area of the internal cross section of the spiral channel was taken to be the same as in the case of Figs. 8–12. The numerical results clearly show that the pressure in spiral at time $t = 0.099$ s (which corresponds to 3000 time steps) reaches a value of 300 bar (Fig. 14). Such flow conditions are inadmissible from the technological viewpoint because they lead to the destruction of the drilling device.

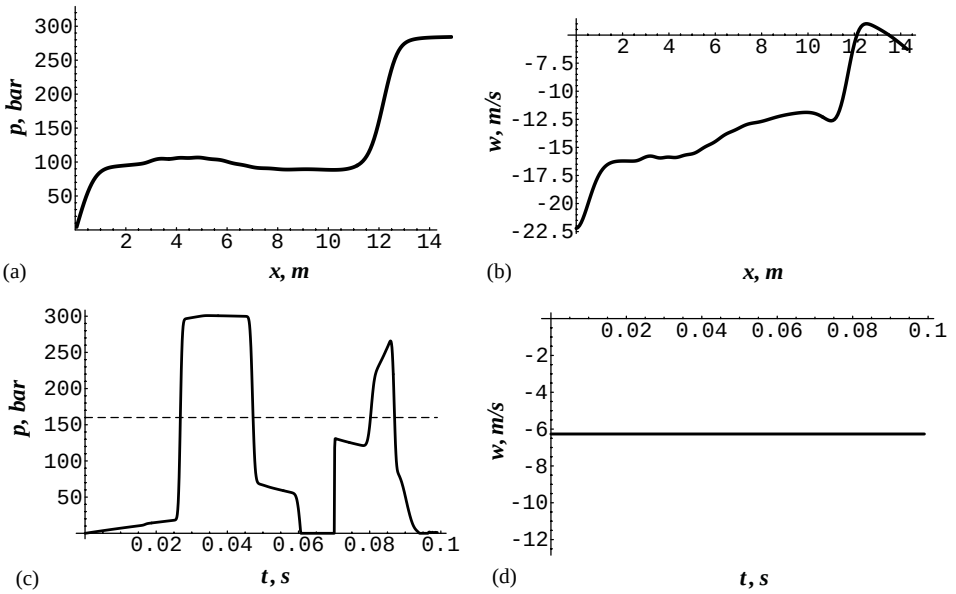

Fig. 14. Numerical results for the pressure and velocity at a fixed flow rate computed by the Ostapenko's scheme: (a) the pressure distribution along the spiral channel at $t = 0.099$ s; (b) the fluid velocity along the spiral channel at $t = 0.099$ s; (c) the pressure versus time at the spiral outlet $\bar{x} = 1$; (d) the velocity versus time at the spiral outlet $\bar{x} = 1$.

7. Conclusions

The purpose of the present work is the numerical modelling and the determination of the optimal design of spiral pressure compensators for the percussion–rotary drills. On the basis of the one-dimensional model and efficient finite difference methods, the nonstationary pressure and flow processes were investigated in the first approximation in such flow channel for the case of periodic pressure shocks (boundary conditions). The following conclusions can be drawn from the conducted numerical computations and analysis:

1. An optimal damping of periodic pressure shocks can be ensured, for a given flow rate Q_0, by a correct choice of the area of the rectangular free flow cross section A. For a given area A of cross section, the damping effect increases when the channel width is larger than its height and when each channel turn lies close to the neighbouring turns ($\psi = 1$ in (2)).

2. The damping effect can be enhanced further by the smoothing of the pressure profile $p_0(t)$ at the spiral inlet. The present authors, therefore, propose to install an additional valve with spring, which is opened by pressure shocks not instantaneously, but with a certain adjusted delay.

The one-dimensional model does not take into account a complex propagation and reflection of shock waves in a strongly curved channel. The actual damping effect, which is encountered in practice, is therefore always stronger than that computed in the present work. For this reason, the one-dimensional numerical model must be generalized for the case of a three-dimensional model. This work is now in progress.

Further research is needed in the domain of the mathematical modelling of cavity phenomena in spiral channel. They are related especially to the phenomena, which involve the formation of gas bubbles in the fluid.

References

Abramovich, G.N., 1991. Applied Gas Dynamics, Part. I. Nauka, Moscow. (in Russian).

Aki, T., 1989. A TVD-scheme study on nonstationary shock reflection. In: Chushkin, P.I., Korobeinikov, V.P. (Eds.), Proceedings of the Soviet Union–Japan Symposium on Computational Fluid Dynamics, Khabarovsk, Vol. 1, 9–16, IX, 1988. Computing Centre of the USSR Academy of Sciences, Moscow, 1989, pp. 154–160.

Arora, M., Roe, P.L., 1997. A well-behaved TVD limiter for high-resolution calculations of unsteady flow. J. Comput. Phys. 132, 3–11.

Blaschke, W., 1950. Einführung in die Differentialgeometrie. Springer, Berlin, Heidelberg.

Bushgens, S.S., 1940. Differential Geometry. Gosud. izdatelstvo tehniko-teoreticheskoi literatury, Moscow, Leningrad. (in Russian).

Daiguji, H., Yuan, H., Yamamoto, S., 1997. Stabilization of higher-order high resolution schemes for the compressible Navier–Stokes equations. Int. J. Numer. Methods Heat Fluid Flow 7, 250–274.

Harten, A., 1983. High resolution schemes for hyperbolic conservation laws. J. Comput. Phys. 49, 357–393.

Harten, A., Osher, S., 1987. Uniformly high-order accurate nonoscillatory schemes. SIAM J. Numer. Anal. 24, 279–309.

Jacob, V.G., 1977. Theory and Calculation on the Working Progress of Hydraulical Drilling Machine. Nedra Press, Moscow.

Jameson, A., Schmidt, W., Turkel, E., 1981. Numerical solution of the Euler equations by finite volume methods using Runge–Kutta time stepping schemes. AIAA Paper 81-1259.

Jenkner, W.R., 1971. Über die Druckstossgeschwindigkeit in Rohrleitungen mit quadratischen und rechteckigen Querschnitten. Schweizerische Bauzeitung. Heft 5, 99–103.

LeVeque, R.J., 1992. Numerical Methods for Conservation Laws. Birkhäuser, Basel, Boston.

LeVeque, R.J., Yee, H.C., 1990. A study of numerical methods for hyperbolic conservation laws with stiff source terms. J. Comput. Phys. 86, 187–210.

Merenkov, A.P., Sennova, E.V., Sumarokov, S.V., Sidler, S.V., Novitskiy, N.N., Stennikov, V.A., Chupin, V.R., 1992. Mathematical Modeling and Optimization of the Systems for Heat, Water, Oil and Gas Supply. Nauka, Novosibirsk (in Russian).

Ostapenko, V.V., 1997. Convergence of finite-difference schemes behind a shock front. Comput. Math. Math. Phys. (Translated from the Russian) 37, 1161–1172.

Ostapenko, V.V., 1999. Numerical simulation of wave flows caused by the shoreside landslide. Appl. Mech. Tech. Phys. (Translated from the Russian) 40, 647–654.

Roache, P.J., 1976. Computational Fluid Dynamics. Hermosa, Albuquerque, NM.

Rožděstvenskii, B.L., Yanenko, N.N., 1983. Systems of Quasilinear Equations and their Applications to Gas Dynamics. American Mathematical Society, Providence, RI.

Swaffield, J.A., Boldy, A.P., 1993. Pressure Surge in Pipe and Duct Systems. Avebury Technical, Aldershot, Brookfield, USA, Hong Kong, Singapore, Sydney.

Takakura, Y., Ishiguro, T., Ogawa, S., 1989. On TVD difference schemes for the three-dimensional Euler equations in general co-ordinates. Int. J. Numer. Methods Fluids 9, 1011–1024.

Toro, E.F., 1999. Riemann Solvers and Numerical Methods for Fluid Dynamics. A Practical Introduction, 2nd Edition. Springer, Berlin, New York.

Van Leer, B., 1979. Toward the ultimate conservative difference scheme. V. A second-order sequel to Godunov's method. J. Comput. Phys. 32, 101–136.

Voevodin, A.F., Shugrin, S.M., 1981. Numerical Methods for Calculating One-Dimensional Systems. Nauka, Siberian Branch, Novosibirsk (in Russian).

Yee, H.C., Harten, A., 1987. Implicit TVD schemes for hyperbolic conservation laws in curvilinear coordinates. AIAA J. 25, 266–274.

Yee, H.C., Warming, R.F., Harten, A., 1985. Implicit total variation diminishing (TVD) schemes for steady-state calculations. J. Comput. Phys. 57, 327–360.

Yee, H.C., Sandham, N.D., Djomehri, M.J., 1999. Low-dissipative high-order shock-capturing methods using characteristic-based filters. J. Comput. Phys. 150, 199–238.

Zhao, G., 1998. Entwicklung und Optimierung eines hydraulischen Bohrhammers. Mitteilungen aus dem Institut für Erdöl-und Erdgastechnik der Technischen Universität Clausthal, Clausthal-Zellerfeld.